PLOS ONE

RESEARCH ARTICLE

Multi-objective optimisation of material properties and strut geometry for poly(L-lactic acid) coronary stents using response surface methodology

Ross W. Blair[1]*, **Nicholas J. Dunne**[2,3,4,5,6], **Alex B. Lennon**[1], **Gary H. Menary**[1]

1 School of Mechanical and Aerospace Engineering, Queen's University, Belfast, United Kingdom, **2** School of Mechanical and Manufacturing Engineering, Dublin City University, Dublin, Ireland, **3** Centre for Medical Engineering Research, School of Mechanical and Manufacturing Engineering, Dublin City University, Dublin, Ireland, **4** School of Pharmacy, Queen's University, Belfast, United Kingdom, **5** Trinity Centre for Bioengineering, Trinity College Dublin, Dublin, Ireland, **6** Advanced Materials and Bioengineering Research Centre (AMBER), Royal College of Surgeons in Ireland and Trinity College Dublin, Dublin, Ireland

* rblair522@qub.ac.uk

Citation: Blair RW, Dunne NJ, Lennon AB, Menary GH (2019) Multi-objective optimisation of material properties and strut geometry for poly(L-lactic acid) coronary stents using response surface methodology. PLoS ONE 14(8): e0218768. https://doi.org/10.1371/journal.pone.0218768

Editor: Yanyu Chen, University of Louisville, UNITED STATES

Received: June 8, 2019

Accepted: August 10, 2019

Published: August 26, 2019

Data Availability Statement: All relevant data is contained within the manuscript.

Funding: The authors wish to acknowledge funding from the Engineering and Physical Sciences Research Council (EPSRC) (S3804ASA) and the Marie Skłodowska-Curie Research and Innovation Staff Exchange (RISE), grant agreement 691238. The funders had no role in study design, data collection and analysis, decision to publish, or preparation of the manuscript.

Abstract

Coronary stents for treating atherosclerosis are traditionally manufactured from metallic alloys. However, metal stents permanently reside in the body and may trigger undesirable immunological responses. Bioresorbable polymer stents can provide a temporary scaffold that resorbs once the artery heals but are mechanically inferior, requiring thicker struts for equivalent radial support, which may increase thrombosis risk. This study addresses the challenge of designing mechanically effective but sufficiently thin poly(L-lactic acid) stents through a computational approach that optimises material properties and stent geometry. Forty parametric stent designs were generated: cross-sectional area (post-dilation), foreshortening, stent-to-artery ratio and radial collapse pressure were evaluated computationally using finite element analysis. Response surface methodology was used to identify performance trade-offs by formulating relationships between design parameters and response variables. Multi-objective optimisation was used to identify suitable stent designs from approximated Pareto fronts and an optimal design is proposed that offers comparable performance to designs in clinical practice. In summary, a computational framework has been developed that has potential application in the design of high stiffness, thin strut polymeric stents.

1. Introduction

Balloon angioplasty, performed by Andreas Grüntzig in 1977, is recorded as the first successful effort to treat an occluded coronary artery and subsequently revolutionised the treatment of coronary artery disease [1]. However, the surgical procedure suffers from significant limitations, namely vessel occlusion and restenosis, which prompted the development of the first

Competing interests: The authors have declared that no competing interests exist.

bare metal stent (*BMS*) nearly a decade later [2]. Whilst *BMSs* reduced the incidence rate of restenosis when compared to balloon angioplasty, the introduction of a permanent metallic cage provoked neointimal hyperplasia, an inflammatory response of the vessel walls [3], and as a result drug-eluting stents (*DESs*) succeeded *BMSs*, containing a durable polymer coating which releases an antiproliferative drug (e.g. sirolimus or paclitaxel) that attenuates intra-stent neointimal proliferation [4]. Drug-eluting stents have shown reduced restenosis rates when compared to *BMSs* [5,6]. However, they suffer from inherent flaws based on the permanent nature of their design and issues have been reported regarding the long-term (> 1 year) safety of these devices including delayed healing and late stent thrombosis (*LST*) [7,8,9], which has prompted the development of bioresorbable stents (*BRSs*). Bioresorbable stents provide short-term scaffolding to the arterial wall until it has healed and are subsequently resorbed, offering superior conformability and flexibility to their permanent metallic counterparts, whilst enabling late luminal gain, late expansive remodelling and potentially reducing the risk of *LST* associated with *DESs* following resorption [10,11].

Whilst polymeric *BRSs* present a clinically attractive option, they require wider and thicker struts to provide an equivalent level of arterial support (Table 1) when compared to their metallic counterparts. As a result, polymeric *BRSs* have higher stent-to-artery ratios [12,13] and have been shown to increase the risk of short-term (< 1 year following implantation) myocardial infarction, thrombosis and restenosis [14,15]. Hence, focus must first be placed on improving the short-term clinical outcomes for polymeric *BRSs*, before addressing long-term (> 1 year following implantation) issues that may arise as the stent degrades and its mechanical integrity deteriorates. A thick-strut design also limits the diameter a stent can be crimped to, resulting in an increased crossing-profile that hinders the deliverability of the device [16] and restrict normal vasomotion [4]. Additionally, polymeric *BRS*s demonstrate higher degrees of foreshortening (due to an increased strut length) during deployment, which can initiate vascular restenosis injuries [17]. Improvements in material processing, coupled with the correct matching of the stent geometry to the material may produce polymeric *BRSs* with reduced strut thickness and comparable performance to current generation metallic *DES* [18–20].

The elastic modulus of the polymer, which affects the radial collapse pressure of the stent, may potentially be the most important parameter in polymeric *BRS* design [20,26]. Pauck and Reddy [20] performed computational bench testing on three commercially available stent geometries, whilst varying the elastic modulus of the platform material, poly(L-lactic acid) (*PLLA*). The authors concluded that using a geometry similar to that of the Absorb *BVS* (Abbott Vascular, USA), with a strut thickness and a strut width of 100 μm, coupled with an elastic modulus of 9 GPa, allows the desired collapse pressure of at least 40 kPa to be met [18]. The elastic modulus of extruded *PLLA* is approximately 3 GPa [27], which is significantly lower than the required value of 9 GPa, and hence additional processing steps must be taken to improve upon this.

Stretch blow moulding (*SBM*) is a processing technique used in the production of *BRS* to improve the elastic modulus of the polymer [27,28]. In the SBM process, the polymer is

Table 1. Comparison of strut geometry and performance metrics of clinically tested bioresorbable stents (*BRSs*) and modern metallic drug-eluting stents (*DESs*) for coronary application [4,12,20–25].

	Polymeric BRSs	*Metallic DESs*
Strut thickness (μm)	125–156	80–140
Strut width (μm)	140–216	80–132
Stent-to-artery ratio (%)	26.0–32.0	15.5–21.4
Crossing profile (mm)	1.2–1.7	1.0–1.2

https://doi.org/10.1371/journal.pone.0218768.t001

initially extruded into a thick-walled tube (parison) and heated above its glass transition temperature during which it is biaxially stretched to create a thin-walled tube with improved mechanical properties [29]. Whilst a three-fold increase in the elastic modulus is difficult to physically attain, Blair et al. [30] showed that by tailoring processing parameters, biaxial stretching can improve the elastic modulus and yield strength of extruded *PLLA* sheet by approximately 80% and 70%, respectively. Given that the relationship between elastic modulus and strut thickness has been shown to be nonlinear [26], through careful matching of material properties to stent geometry, a physically attainable elastic modulus may be used to meet the radial stiffness threshold with a minimal increase in strut thickness.

The mechanical performance and efficacy of a stent design is strongly dependent on the configuration of strut geometry [31–33]. Finite element analysis is an especially prevalent technique within the discipline of computational biomechanics, where *in vivo* testing is exceptionally challenging, and may be used as preclinical testing tool to optimise stent geometry prior to any form of physical testing [31,34]. To evaluate the performance and efficacy of a given stent design, simulated tests are typically conducted in which one (or more) metrics are assessed across a range of potentially viable stent geometries. Stent geometries may be parameterised in terms of strut width, strut thickness, strut length and connector shape [35] whilst performance metrics fall under two main headings: (i) dilation metrics and (ii) mechanical metrics. Dilation metrics are concerned with the behaviour of the stent during (and immediately following) inflation, with radial recoil, foreshortening and stent-to-artery ratio amongst the most commonly evaluated metrics [32,36]. Mechanical metrics are concerned with the performance of the expanded stent, with radial stiffness considered as the most important mechanical metric for polymeric stents [20].

It is difficult to define what constitutes an optimal stent design, given that the definition of 'optimal' depends on the parameters investigated and the performance metrics assessed. The ideal stent is typically considered as one that is highly deliverable with thin-struts (to improve delivery through tortuous vascular paths) but with high radial stiffness and minimal elastic recoil, to resist restenosis [37]. However, this statement in itself presents a number of conflicting requirements and as a result, an optimised design will always be a trade-off. This is evident from a cross-comparison of the parametric studies conducted by García et al. [38], Li et al. [39], Migliavacca et al. [32], Pant et al. [40] and Timmins et al [41]. Radial stiffness and radial recoil were improved by increasing strut width and strut thickness whilst decreasing strut length, however this often came at the expense of the stent-to-artery ratio and foreshortening.

In summary, improvements in *PLLA* stent design may be attained using a combination of two factors: (i) enhancing mechanical properties of the platform polymer by tailoring its processing history and (ii) iteratively refining the stent's shape by modifying key geometric features. Few studies have considered the combined effect of the processing history and stent geometry in order to optimise stent performance [39,42]. Furthermore, to the best of the authors' knowledge, no study has considered the combined effect of the biaxial stretching processing history and the geometric configuration when optimising the mechanical performance of a *PLLA* coronary stent. This study aims to address this challenge of designing mechanically effective but sufficiently thin bioresorbable *PLLA* stents through multi-objective optimisation of material parameters and stent geometry.

2. Material and methods

The design of *PLLA* stents may be improved by enhancing the material properties of the platform polymer through biaxial stretching and iteratively refining the stent geometry. By parameterising these design inputs and computationally evaluating the performance of a given

stent design across a series of metrics (that capture the conflicting requirements for a stent), empirical relations were derived that relate both the stent's processing history and geometry to its performance. Using these empirical relations, performance trade-offs were identified and an optimal design was established through multi-objective optimisation.

2.1 Process parameterisation

In a previous study by Blair et al. [30], the *SBM* process (used during stent manufacture) was idealised and replicated using a custom-built biaxial tensile tester, to evaluate the mechanical properties of *PLLA* pre- and post-biaxial stretching. The elastic modulus (E) and yield strength (σ_Y) of extruded PLLA sheet increased by approximately 80% and 70% following biaxial stretching (Fig 1a). These mechanical properties were observed to be highly dependent on the stretch ratio in the machine direction (*MD*), λ_{MD}, and the stretch ratio in the transverse direction (*TD*), λ_{TD}, in addition to the aspect ratio (A_r) between the pair, defined as the quotient of λ_{TD} and λ_{MD} (Fig 1b). By tailoring A_r, biaxially stretched sheets were processed with direction dependent (anisotropic) mechanical properties. For $A_r > 1$, i.e. $\lambda_{TD} > \lambda_{MD}$, mechanical properties were improved in the TD at the expense of the mechanical properties in the MD. For $A_r < 1$, i.e. $\lambda_{TD} < \lambda_{MD}$, mechanical properties were improved in the MD at the expense of the mechanical properties in the TD. Therefore, it was hypothesised that if the *MD* and the *TD* were aligned with the stent's axial and circumferential axes, respectively (Fig 1c), a stent may be made stiffer and stronger in a given direction by tailoring A_r.

In a follow-on study, Blair et al. [43] varied A_r and performed uniaxial tensile testing at comparable conditions to those experienced by a stent [44]. Results showed that the elastic modulus and yield strength were strongly dependent on temperature during uniaxial deformation, but were not heavily dependent on extension rate. Empirical relations were developed that related the elastic modulus and yield strength to A_r and temperature (for $A_r \geq 1$). In the present study, a constant body temperature was assumed (37 ˚C) and these equations were simplified for $A_r \geq 1$ (Eqs 1–4) and rearranged for $A_r < 1$ (Eqs 5–8). This set of empirical relations was used to generate a simplified transversely isotropic, rate-independent, elastic-plastic constitutive model [43], which neglects the softening following yield and assumes *PLLA* exhibits perfectly plastic behaviour, i.e. a change in strain causes no observable change in stress (Fig 2a–2c). In the context of a stent, an $A_r = 1$ generated a design of equal strength and stiffness in both the axial and circumferential directions (Fig 2a). An $A_r < 1$ generated a design that was stiffer and stronger in the axial direction (Fig 2b), whilst $A_r > 1$ generated a design that was stiffer and stronger in the circumferential direction (Fig 2c). Given that one of the most challenging aspects to overcome when designing polymer-based stents lies in the significantly

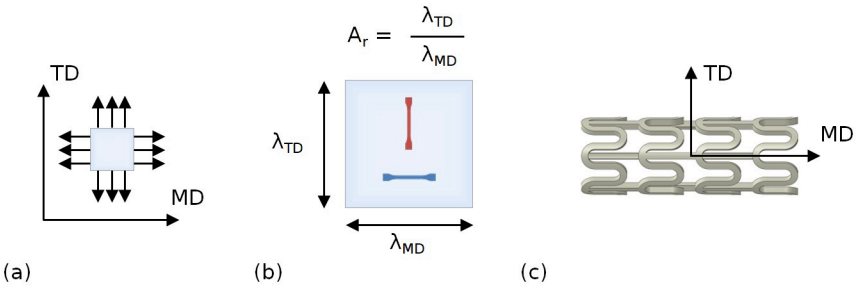

Fig 1. Schematic diagram showing (a) the biaxial stretching process in the machine direction (*MD*) and transverse direction (*TD*); (b) the definition of aspect ratio (A_r), defined as the quotient of the stretch ratio in the TD (λ_{TD}) and and the stretch ratio in the MD (λ_{MD}) and; (c) the alignment of the *MD* and the *TD* with a stent's axial and circumferential axes, respectively.

https://doi.org/10.1371/journal.pone.0218768.g001

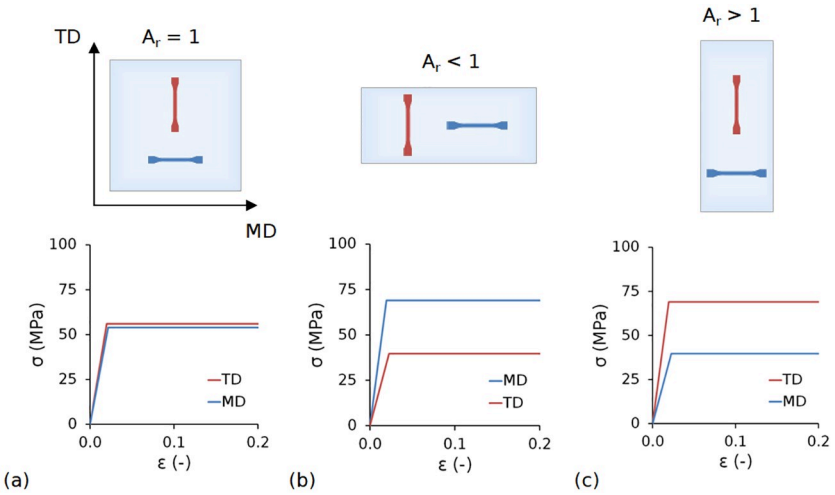

Fig 2. Constitutive model stress-strain (σ-ε) curves for (a) $A_r = 1$, which generated a stent design of equal strength and stiffness in both the axial and circumferential directions; (b) $A_r < 1$, which generated a stent design that was stiffer and stronger in the axial direction; and (c) $A_r > 1$, which generated a stent design that was stiffer and stronger in the circumferential direction.

https://doi.org/10.1371/journal.pone.0218768.g002

lower radial stiffness compared to their metallic counterparts, it may be beneficial to process the stent such that it has a preferential circumferential orientation.

For $A_r \geq 1$:

$$E_{MD} = 3062 - 555A_r \tag{1}$$

$$E_{TD} = 2196 + 618A_r \tag{2}$$

$$\sigma_{Y,MD} = 65 - 11A_r \tag{3}$$

$$\sigma_{Y,TD} = 46 + 10A_r \tag{4}$$

For $A_r < 1$:

$$E_{MD} = 2196 + \frac{618}{A_r} \tag{5}$$

$$E_{TD} = 3062 - \frac{555}{A_r} \tag{6}$$

$$\sigma_{Y,MD} = 46 + \frac{10}{A_r} \tag{7}$$

$$\sigma_{Y,TD} = 65 - \frac{11}{A_r} \tag{8}$$

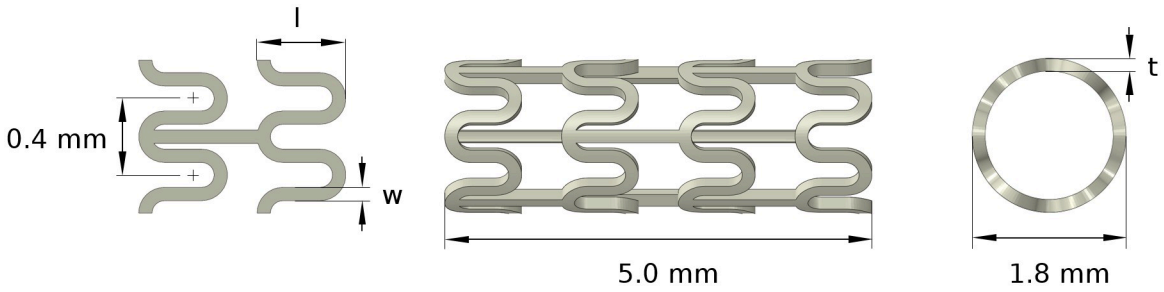

Fig 3. Geometry parameterisation in terms of strut width (*w*), strut thickness (*t*) and strut length (*l*).

https://doi.org/10.1371/journal.pone.0218768.g003

2.2 Geometry parametrisation

The stent geometry used in the present study was based on a conventional open-cell stent design with straight bridges, using SolidWorks 2016 (Dassault Systèmes, France) to generate the three-dimensional model (Fig 3). The stent was designed in the crimped state with two repeating unit cells used to represent the full-length stent geometry, thereby reducing computational cost. Parametric stent geometries were generated by varying the strut width (*w*), the strut thickness (*t*) and the strut length (*l*).

2.3 Performance metrics

Four performance metrics were extracted for each stent design, based on the results of deployment and bench test simulations: (i) the cross-sectional area post-dilation (*CSA*), (ii) foreshortening (*FS*), (iii) stent-to-artery ratio (*SAR*) and (iv) radial collapse pressure (*RCP*). Initially, an idealised quasi-static expansion procedure was simulated in Abaqus/Standard 2016 (Dassault Systèmes, France) using a displacement driven cylinder (meshed with S4R shell elements) and a deformable solid stent (meshed with C3D8R brick elements). The stent was designed in a pre-crimped state (Fig 4a) and constrained in both the axial and tangential directions (with respect to a user-defined cylindrical coordinate system) via three nodes forming an equilateral triangle in the central section. A radial displacement was prescribed to all nodes on the cylinder increasing the stent diameter from 1.8 mm to 3.5 mm using the smooth-step amplitude definition within Abaqus, with tangential and axial displacement prohibited (Fig 4b). Frictionless surface-to-surface contact was assumed, and self-contact was enabled for the stent. Following expansion, the cylinder was contracted during which the stent recoiled (Fig 4c). The timeframe typically required for polymeric stent expansion approaches 1 min according to

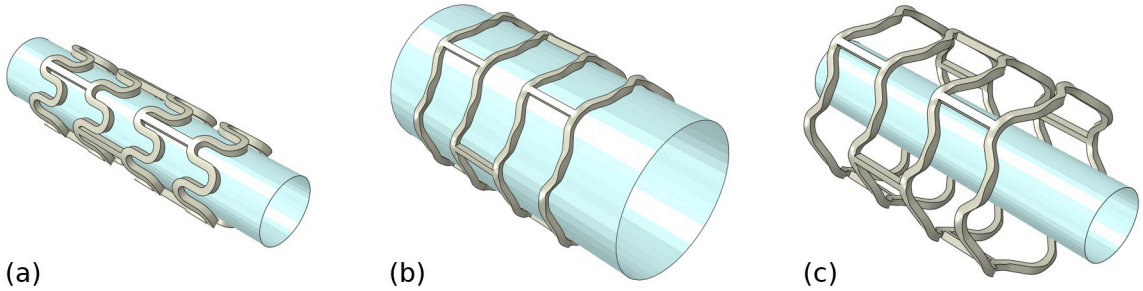

Fig 4. Finite element deployment simulation showing the stent in its (a) initial crimped state; (b) deployed (expanded) state and (c) final (recoiled) state.

https://doi.org/10.1371/journal.pone.0218768.g004

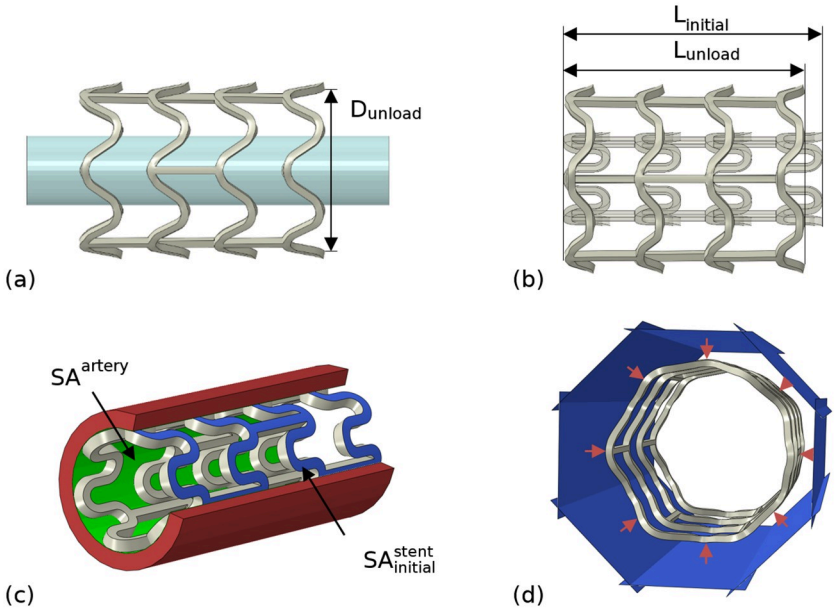

Fig 5. Schematic representations of tests for: (a) cross-sectional area (post-dilation), *CSA*; (b) foreshortening, *FS*; (c) stent-to-artery ratio, *SAR* and (d) radial collapse pressure, *RCP*.

https://doi.org/10.1371/journal.pone.0218768.g005

published guidelines from Abbott [45]. However, given that a rate-independent material model is used, the time frame for expansion was reduced to 1 s.

The *CSA* following unloading was calculated based on the internal diameter of the stent (D_{unload}) (Eq 9) (Fig 5a). During expansion, the opening of the strut hoops naturally cause the stent to contract in the axial direction (Fig 5b). The *FS* of a stent was defined as the percentage reduction between the stent length in its crimped state ($L_{initial}$) and the stent length following unloading (L_{unload}) (Eq 10). The *SAR* of the stent (Fig 5c) was calculated as the ratio between the external surface area of the stent in its crimped state ($SA^{stent}_{initial}$) and the internal surface area of a compatible cylindrical artery (SA^{artery}) (Eq 11). The *RCP* of an expanded stent was evaluated through an additional virtual bench test in which eight rigid plates (meshed with R3D4 elements) (Fig 5d) were radially contracted using a displacement driven process to produce 10% diameter loss. The *RCP* was calculated as the quotient of the average reaction force acting on the plates (RF_{ave}) and the surface area of the stent post-recoil (SA^{stent}_{unload}) (Eq 12). The smooth-step amplitude definition was used with frictionless surface-to-surface contact between the plates and the stent, and self-contact was enabled for the stent.

$$CSA = \pi\left(\frac{D_{unload}}{2}\right)^2 \tag{9}$$

$$FS = \frac{L_{initial} - L_{unload}}{L_{initial}} \times 100\% \tag{10}$$

$$SAR = \frac{SA^{stent}_{initial}}{SA^{artery}} \times 100\% \tag{11}$$

$$RCP = \frac{RF_{ave}}{SA_{unload}^{stent}} \quad (12)$$

2.4 Optimisation

The time required to perform the finite element simulations and calculate the performance metrics for a given parametric stent design exceeded 1 h using five parallel processors. At these time scales, global optimisation processes become computationally inefficient and the majority of optimisation studies tend to adopt surrogate modelling approaches [35]. Hence, response surface methodology (*RSM*) was employed to provide an empirical correlation between processing and geometry parameters and the mechanical performance of the stent.

A design space was established using the limits for each of the design parameters (Table 2). The lower limit of A_r generates stents that are stiffer in the axial direction whilst the upper limit generates stents that are stiffer in the circumferential direction. A lower limit of 100 μm was set for w and t to generate geometries that resembled a metallic stent, whilst an upper limit of 200 μm was set to generate geometries that resembled a polymeric stent. An upper limit of 1200 μm was set for l to avoid self-contact between neighbouring circumferential rings, whilst a lower limit of 900 μm was set to prevent excessive plastic deformation. A baseline design was generated by setting A_r, w, t and l at the midpoint of their range.

Initially, 40 design points that uniformly filled the design space were selected using an optimised Latin hypercube (LHC) sampling technique [46]. Parametric stent designs and finite element models were automatically generated using a combination of Python (version 2.7.13; Python Software Foundation) scripting, SolidWorks 2016 and the Abaqus CAE pre-processor. Deployment and bench testing simulations were performed in order to compute discrete values for each performance metric (*CSA*, *FS*, *SAR* and *RCP*). Multiple linear regression analysis was performed on the results using R (version 3.4.0) [47] to provide an empirical correlation between each performance metric and design parameters. The Matplotlib (version 2.2.2) package [48] was used to generate three-dimensional response surface plots to provide a qualitative, visual assessment of the results.

Following the RSM, multi-objective sequential least squares optimisation was performed in Python using the NumPy (version 1.14.2) [49] and SciPy packages (version 1.2.0) [50] to identify suitable options from non-dominated Pareto designs, i.e. a design that cannot be improved without degrading at least one of the other performance metrics. Each performance metric was normalised (scaled) to the same range [0,1], based on its minimum and maximum attainable values, attained through single objective sequential least squares minimisation. A single objective function (*OF*) was constructed (Eq 13) that combines these normalised *CSA*, *FS*, *SAR* and *RCP* terms. Each of these performance metrics have been shown to directly affect one (or more) of the commonly assessed clinical outcomes for a stent. A low *CSA* may restrict normal vasomotion [4], a high degree of *FS* may initiate restenosis [17], a high *SAR* may initiate thrombosis [15], whilst a low *RCP* may prevent the stent from withstanding the compressive force of the artery [37]. Hence, an equal weighting was applied to the normalised *CSA*, *FS*, *SAR* and *RCP* terms. The intention of this optimisation was to minimise *FS* and *SAR* whilst maximising *CSA* and *RCP*. Hence, negative sign convention was adopted for *CSA* and *RCP* so

Table 2. High and low levels for design parameters (A_r, w, t and l).

A_r (-)	w (μm)	t (μm)	l (μm)
0.4	100	100	900
2.3	200	200	1,200

https://doi.org/10.1371/journal.pone.0218768.t002

Table 3. Baseline stent design parameters (A_r, w, t, and l) and its respective performance metrics (*CSA*, *FS*, *SAR*, and *RCP*).

A_r (-)	w (μm)	t (μm)	l (μm)	*CSA* (mm^2)	*FS* (%)	*SAR* (%)	*RCP* (kPa)
1.35	150	150	1050	-8.0	5.7	35.3	-20.9

https://doi.org/10.1371/journal.pone.0218768.t003

that lower values for absolute and normalised performance metrics indicate better designs. An inequality constraint was imposed that prevented *RCP* dropping below 40 kPa (Eq 14), which is commonly considered the minimum allowable collapse pressure for coronary stents [18]. An additional inequality constraint was imposed that prevented t from exceeding the baseline value of 150 μm (Eq 15).

$$\min(OF) = \widehat{CSA} + \widehat{FS} + \widehat{SAR} + \widehat{RCP} \tag{13}$$

s.t.

$$RCP \geq 40 \ kPa \tag{14}$$

$$t \leq 150 \ \mu m \tag{15}$$

3. Results

3.1 Baseline geometry

The baseline stent design parameters and the respective performance metrics are shown in Table 3. Cross-sectional area (post-dilation) is difficult to measure *in vivo* and hence, there is limited published data. However, the baseline design recoiled by approximately 9% following dilation, which is comparable to commercial *PLLA BRS* [24]. Given that the value of t is similar between the baseline design and a commercial stent, by extension, the *CSA* will also be comparable. The baseline stent design values for *SAR* and *FS* of 5.7% and 35.5%, respectively, are comparable to the upper end of the commercial *PLLA BRS* range [12,24]. However, the baseline stent value for *RCP* of 20.9 kPa is approximately half of the minimum allowable collapse pressure for a coronary stent [18], thereby justifying the requirement for the present optimisation study.

3.2 Response surface methodology

The four performance metrics (*CSA*, *FS*, *SAR* and *RCP*) were computed for each of the 40 design points (Table 4).

Multiple linear regression analysis was performed to generate constitutive equations that related each performance metric to the input parameters. A second-order model containing the intercept, main factors, two-factor interactions and quadratic terms (Eq 16) was used for *CSA*, *FS*, *SAR* and *RCP*. Using the constants in Table 5, each model predicted, with approximately 99.7% confidence, that all values lie within the mean prediction plus or minus three standard deviations (Fig 6). Model quality is assessed in Fig 7, in which the performance metrics were predicted for a given set of design parameters using the statistical model (Eq 16), and compared to their corresponding actual (measured) values extracted from finite element simulations. Linear behaviour was observed for *CSA*, *FS*, *SAR* and *RCP*, with the statistical models achieving R-squared (R^2) values of 0.950, 0.996, 0.999 and 0.996, respectively.

$$\begin{aligned} Y = {} & \beta_0 + \beta_1 A_r + \beta_2 w + \beta_3 t + \beta_4 l + \beta_5 A_r w + \beta_6 A_r t + \beta_7 A_r l + \\ & \beta_8 wt + \beta_9 wl + \beta_{10} tl + \beta_{11} {A_r}^2 + \beta_{12} w^2 + \beta_{13} t^2 + \beta_{14} l^2 \end{aligned} \tag{16}$$

Table 4. Design parameters (A_r, w, t and l) and respective performance metrics (*CSA*, *FS*, *SAR* and *RCP*) for each point considered under the optimised Latin hypercube sampling plan.

Design	A_r (-)	w (μm)	t (μm)	l (μm)	*CSA* (mm^2)	*FS* (%)	*SAR* (%)	*RCP* (kPa)
1	0.90	101	191	1166	-6.2	3.4	26.7	-6.8
2	0.47	134	161	1001	-8.1	6.8	30.9	-18.9
3	0.52	119	154	1144	-7.0	4.2	30.5	-8.5
4	0.71	124	134	1039	-7.6	5.5	29.9	-13.1
5	2.23	146	169	1009	-8.4	5.8	33.6	-22.8
6	0.61	164	184	1016	-8.4	8.5	37.2	-35.3
7	0.57	179	156	956	-8.8	10.0	38.4	-39.9
8	1.90	189	189	1136	-8.4	6.4	45.5	-32.6
9	1.37	176	104	971	-9.2	7.4	38.3	-23.7
10	1.42	199	126	1084	-8.5	7.2	45.9	-27.7
11	1.94	151	121	1196	-8.1	3.6	39.1	-10.8
12	1.33	116	166	949	-8.1	6.6	26.3	-20.2
13	0.95	139	106	979	-8.6	6.6	31.4	-16.0
14	2.13	186	179	1046	-8.7	7.2	42.4	-36.8
15	1.80	169	146	994	-8.7	6.8	37.6	-29.4
16	1.23	161	176	904	-9.0	9.5	33.8	-45.3
17	1.52	129	144	1189	-6.9	3.1	33.7	-8.8
18	1.61	191	174	941	-9.1	9.5	40.1	-53.9
19	2.04	136	136	964	-8.4	5.8	30.6	-18.1
20	2.18	156	141	1076	-8.9	5.1	37.2	-18.6
21	1.09	194	111	911	-9.0	10.5	39.6	-35.0
22	1.18	141	124	1091	-8.2	4.7	34.4	-13.8
23	2.28	154	164	1174	-7.8	4.1	39.1	-14.5
24	1.28	196	196	1024	-8.8	9.1	43.5	-51.0
25	1.04	184	139	1114	-8.2	6.6	43.9	-24.7
26	1.99	126	114	1054	-7.7	3.9	30.4	-10.5
27	1.47	104	159	1069	-7.0	3.8	25.7	-9.2
28	1.56	131	199	1061	-7.8	4.9	31.6	-20.4
29	2.09	109	151	986	-7.8	4.9	25.4	-12.4
30	0.76	181	109	1129	-8.0	6.7	43.8	-17.4
31	1.75	149	194	934	-8.8	8.0	32.3	-38.0
32	0.66	171	129	919	-8.8	9.7	36.0	-31.6
33	0.99	106	116	926	-7.8	6.1	23.9	-12.9
34	0.42	159	131	1031	-8.9	7.5	36.6	-18.6
35	1.66	114	119	1121	-6.9	3.2	28.9	-6.9
36	1.85	111	186	1151	-6.8	3.2	28.9	-8.7
37	0.80	144	149	1181	-7.2	4.6	37.0	-12.1
38	1.71	166	101	1106	-8.5	5.0	40.1	-14.3
39	0.85	121	171	1099	-7.2	4.7	30.2	-12.7
40	1.14	174	181	1159	-7.9	5.9	43.1	-25.7

https://doi.org/10.1371/journal.pone.0218768.t004

where Y denotes the predicted response for a given performance metric, i.e. *CSA*, *FS*, *SAR* and *RCP*.

A comparison of absolute t-values (for coefficients) from multiple regression analyses for each performance metric is shown in Fig 8. Main factors, two-factor interactions and quadratic

Table 5. Statistical model coefficients for *CSA*, *FS*, *SAR* and *RCP*.

	CSA	*FS*	*SAR*	*RCP*
Intercept	-2.6	44.9	-1.1	-25.3
A_r	16.0E-1	-26.6E-1	-4.7E-1	-69.2E-1
w	-55.7E-3	6.6E-3	96.3E-3	-249.7E-3
t	-2.7E-3	25.3E-3	1.5E-3	-422.3E-3
l	-7.1E-3	-67.5E-3	3.1E-3	110.3E-3
A_r:***w***	-3.8E-3	-6.8E-3	1.5E-3	-2.0E-3
A_r:***t***	7.1E-4	10.4E-4	3.3E-4	183.6E-4
A_r:***l***	-10.6E-4	11.6E-4	1.7E-4	-16.0E-4
w*:*t	2.6E-5	2.6E-5	-1.1E-5	-225.7E-5
w*:*l	-2.3E-5	-1.2E-5	15.9E-5	56.3E-5
t*:*l	9.8E-6	-35.7E-6	-4.2E-6	612.6E-6
A_r^2	-7.5E-2	48.5E-2	1.3E-2	251.7E-2
w^2	2.2E-4	1.8E-4	-2.0E-4	-9.3E-4
t^2	-3.6E-5	5.8E-5	1.2E-5	-22.5E-5
l^2	7.3E-6	27.9E-6	-1.3E-6	-104.5E-6

https://doi.org/10.1371/journal.pone.0218768.t005

terms are considered statistically significant ($p < 0.05$) if their absolute t-value lies above the dashed line.

Response surfaces were plotted for all two-way interactions (Figs 9–14), which highlight the combined influence of any two design parameters (A_r, w, t or l) on each performance metric (*CSA*, *FS*, *SAR* and *RCP*). For each response surface, the performance metric was plotted against two dependent design parameters whilst the remaining two independent parameters were held constant at their baseline (midpoint) value. For each response surface, moving from the purple region to the yellow region indicates an improvement.

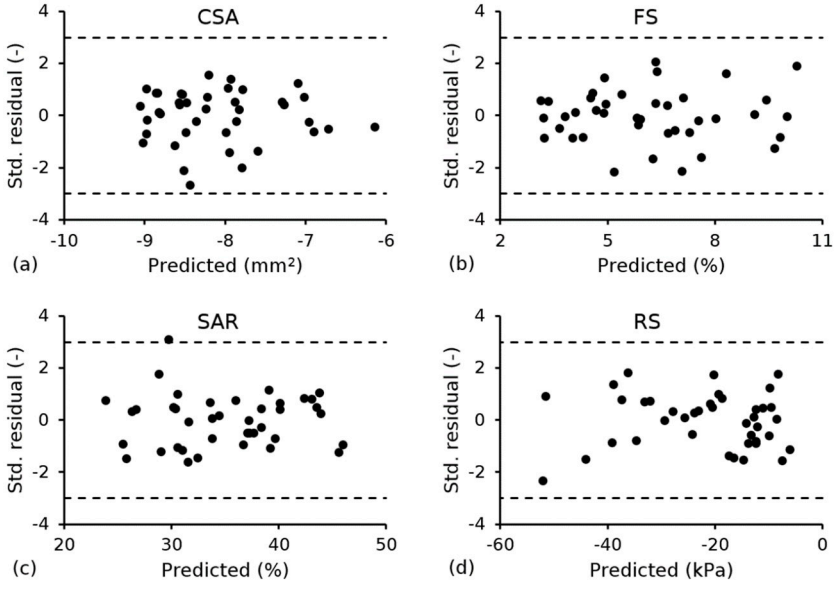

Fig 6. Standardised residual *vs*. predicted response using the statistical model in Eq 16 for (a) *CSA*; (b) *FS*; (c) *SAR* and (d) *RCP*.

https://doi.org/10.1371/journal.pone.0218768.g006

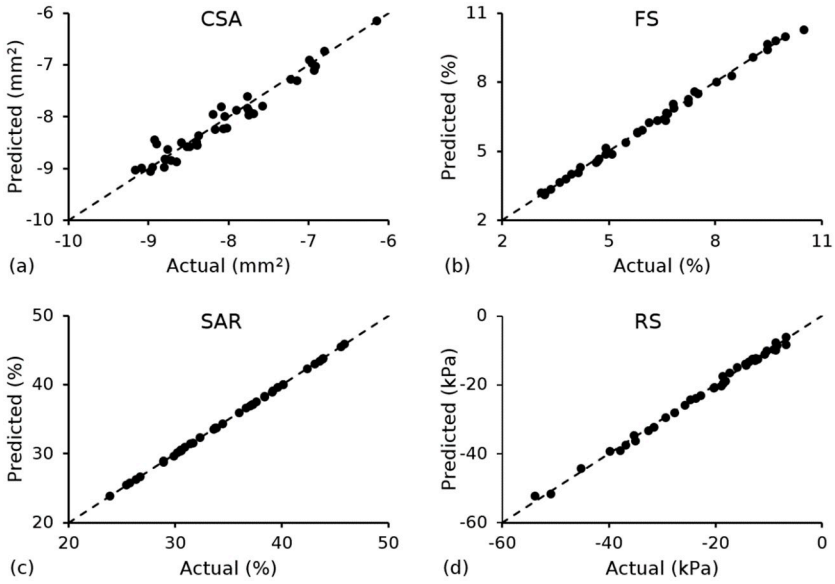

Fig 7. Predicted response using the statistical model in Eq 16 vs. actual (measured) response from finite element simulations for (a) *CSA*; (b) *FS*; (c) *SAR* and (d) *RCP*.

https://doi.org/10.1371/journal.pone.0218768.g007

The Pareto fronts (Fig 15) highlight the trade-offs between each set of performance metrics, with better designs lying towards the bottom left corner. Trade-offs were observed for *CSA vs. FS*, *CSA vs. SAR*, *FS vs. RCP* and *SAR vs. RCP*, whilst no trade-offs were observed for *CSA vs. RCP* or *FS vs. SAR*. Trade-offs occurred as a result of conflicting requirements for stent design, i.e. geometric and/or material parameters that improve one metric often negatively affect at least one of the other metrics.

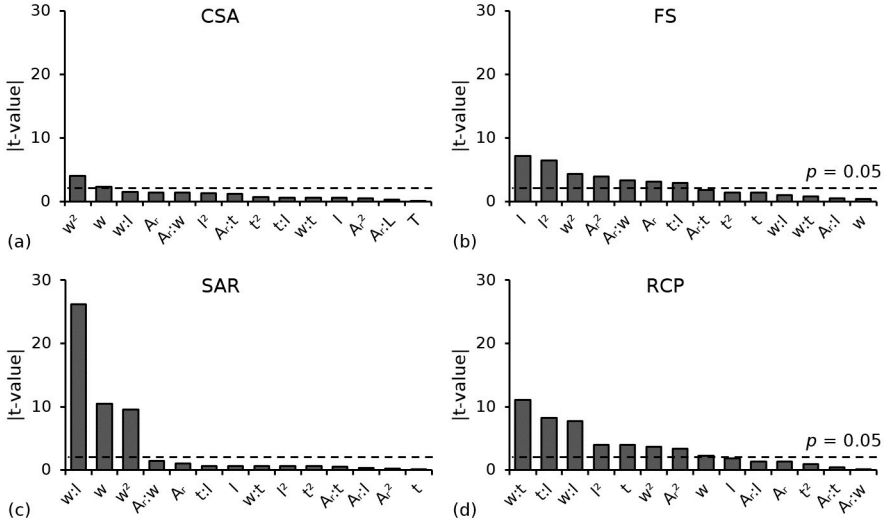

Fig 8. Comparison of absolute t-values (for coefficients) from multiple regression analyses highlighting significant ($p < 0.05$) main factors and two-way interactions for (a) *CSA*; (b) *FS*; (c) *SAR* and (d) *RCP*.

https://doi.org/10.1371/journal.pone.0218768.g008

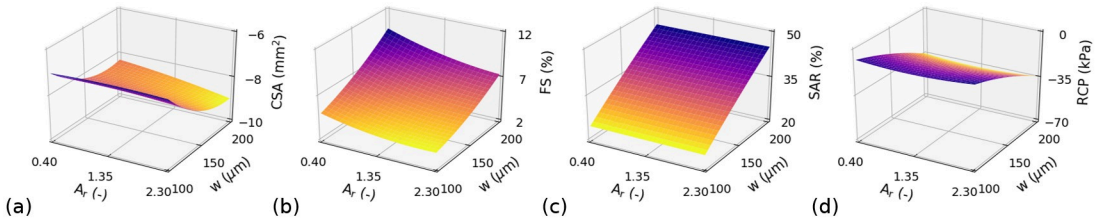

Fig 9. Response surfaces highlighting the combined influence of A_r and w on each performance metric (*CSA*, *FS*, *SAR* and *RCP*), holding t and l constant at their baseline values (t = 150 μm and l = 1050 μm).

https://doi.org/10.1371/journal.pone.0218768.g009

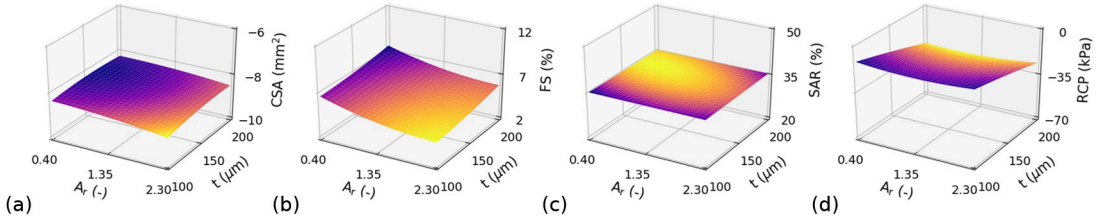

Fig 10. Response surfaces highlighting the combined influence of A_r and t on each performance metric (CSA, FS, SAR and RCP), holding w and l constant at their baseline values (w = 150 μm and l = 1050 μm).

https://doi.org/10.1371/journal.pone.0218768.g010

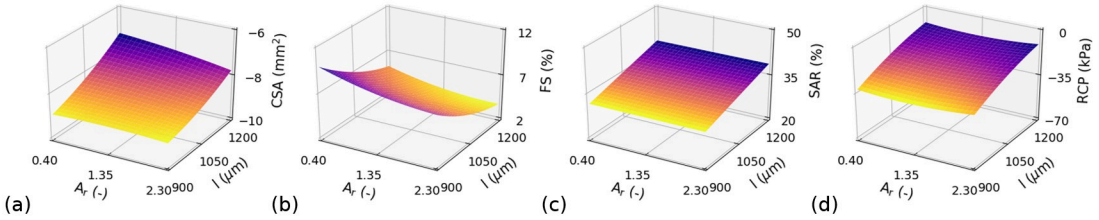

Fig 11. Response surfaces highlighting the combined influence of A_r and l on each performance metric (CSA, FS, SAR and RCP), holding w and t constant at their baseline values (w = 150 μm and t = 150 μm).

https://doi.org/10.1371/journal.pone.0218768.g011

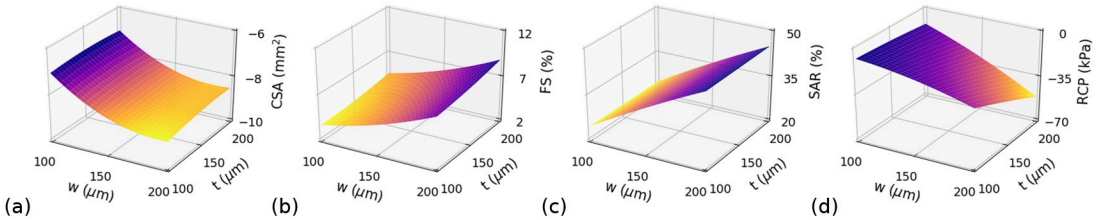

Fig 12. Response surfaces highlighting the combined influence of w and t on each performance metric (CSA, FS, SAR and RCP), holding A_r and l constant at their baseline values (A_r = 1.35 and l = 1050 μm).

https://doi.org/10.1371/journal.pone.0218768.g012

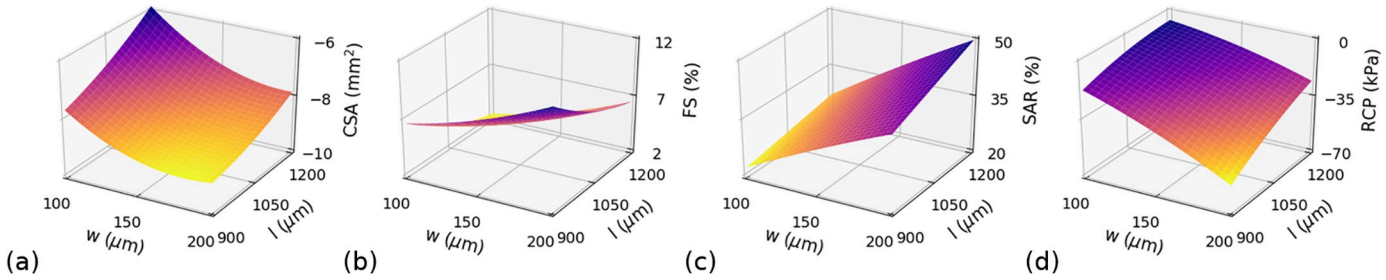

Fig 13. Response surfaces highlighting the combined influence of *w* and *l* on each performance metric (CSA, FS, SAR and RCP), holding A_r and *t* constant at their baseline values (A_r = 1.35 and *t* = 150 μm).

https://doi.org/10.1371/journal.pone.0218768.g013

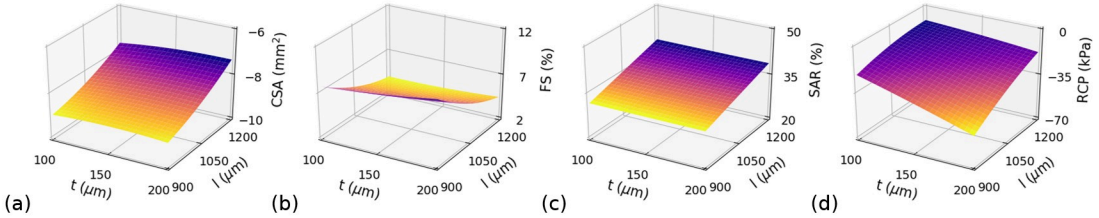

Fig 14. Response surfaces highlighting the combined influence of *t* and *l* on each performance metric (CSA, FS, SAR and RCP), holding A_r and *w* constant at their baseline values (A_r = 1.35 and *w* = 150 μm).

https://doi.org/10.1371/journal.pone.0218768.g014

3.3 Optimisation

To construct a single dimensionless objective function, each performance metric was normalised (scaled) to the same range [0,1] based on its minimum and maximum attainable values (Table 6), attained using least squares minimisation (Eq 17).

$$\hat{Y} = \frac{Y - Y_{min}}{Y_{max} - Y_{min}} \tag{17}$$

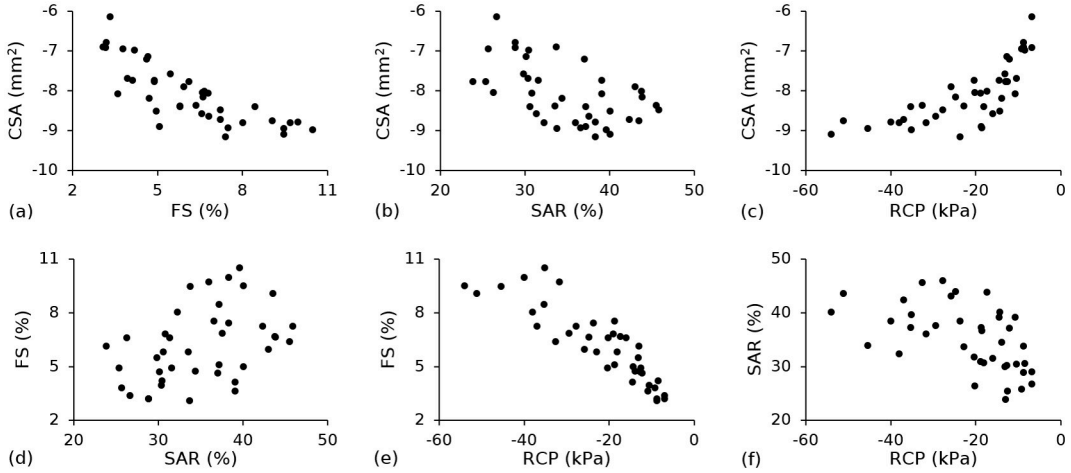

Fig 15. Trade-off curves for all permutations of the four performance metrics: (a) *CSA vs. FS*; (b) *CSA vs. SAR*, (c) *CSA vs. RCP* and (d) *FS vs. SAR*, (e) *FS vs. RCP* and (f) *SAR vs. RCP*.

https://doi.org/10.1371/journal.pone.0218768.g015

Table 6. Minimum and maximum values for each performance metric (*CSA*, *FS*, *SAR* and *RCP*).

	CSA (mm^2)	*FS* (%)	*SAR* (%)	*RCP* (kPa)
Min.	-9.4	2.3	22.1	-72.6
Max.	-5.8	13.9	50.0	-0.7

https://doi.org/10.1371/journal.pone.0218768.t006

Table 7. Comparison between baseline (base.) and optimal (opt.) stent designs highlighting design parameters and their respective performance metrics.

	A_r (-)	*w* (μm)	*t* (μm)	*l* (μm)	*CSA* (mm^2)	*FS* (%)	*SAR* (%)	*RCP* (kPa)
Base.	1.35	150	150	1050	-8	5.7	35.3	-20.9
Opt.	2.3	173	150	900	-9.1	8	35.7	-40

https://doi.org/10.1371/journal.pone.0218768.t007

where $\hat{Y}$ and Y denote the predicted normalised and absolute responses, respectively, for a given performance metric, whilst Y_{min} and Y_{max} denote the minimum and maximum attainable values.

Multi-objective optimisation produced a stent design superior to the baseline with t = 150 μm and w = 173 μm (Table 7), which are lower than some commercial polymeric stents [12], whilst meeting the minimum allowable collapse pressure [18]. A comparison between the baseline design and the optimised design is shown in Fig 16, in which each performance metric has been normalised. The *RCP* of the optimal design is approximately twice that of the baseline design with a less than 1% increase in *SAR*. The *CSA* increased by 14% and whilst *FS* increased, a value of 8% is comparable to stents in commercial use [51].

4. Discussion

This study proposes a multi-objective optimisation framework that considers the combined effect of the biaxial stretching processing history and the geometric configuration when optimising the short-term (pre-degradation) mechanical performance of a *PLLA* coronary stent. Given that the ideal stent must fulfil a range of conflicting technical requirements, a multi-objective optimisation process that offers compromises between key performance metrics was conducted to develop a polymeric stent that offered improved performance relative to a baseline design for the same strut thickness (150 μm). Performance trade-offs were observed (Fig 15) and may be explained using the absolute t-value comparisons for coefficients (Fig 8) and the response surface interaction plots for each performance metric (Figs 9–14). The absolute t-

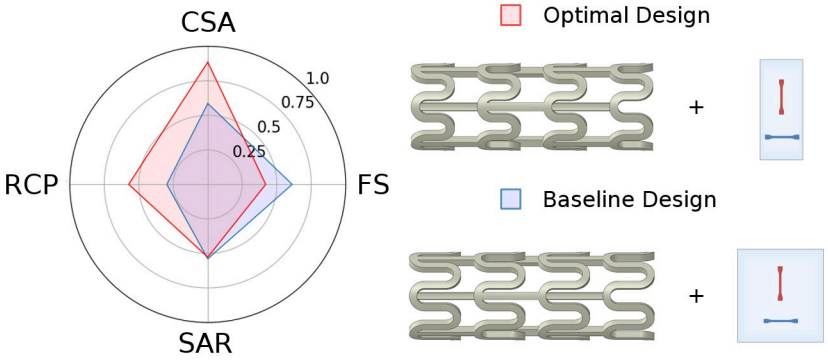

Fig 16. Visual comparison of normalised performance metrics and design parameters between the baseline design and the optimal design.

https://doi.org/10.1371/journal.pone.0218768.g016

value comparisons for coefficients highlight statistically significant ($p < 0.05$) factors for each performance metric whilst the response surface interaction plots provide a visual aid in understanding the interdependent effect between two factors on a given performance metric.

4.1 Cross-sectional area *vs*. foreshortening

The trade-off between *CSA* and *FS* was primarily due to the conflicting requirements for w and *l*. Cross-sectional area was most strongly affected by w and w^2 (Fig 8a), whilst *FS* was most strongly affected by *l* and l^2 (Fig 8b). Increasing *w* improved *CSA* as a wider strut increased plastic deformation in the hoops and reduced radial recoil, which is in agreement with the findings of Pant et al. [40]. Furthermore, the presence of a significant ($p < 0.05$) quadratic effect (w^2) in the model suggested a curvilinear relationship between *CSA* and *w*. This was evident from the interaction plots in which *w* was plotted as one of the dependent variables (Figs 9a, 12a and 13a). A convex relationship was observed between *CSA* and *w*, i.e. *CSA* improved as *w* increased but with diminishing returns. Decreasing *l* further improved *CSA* and was evident from the interaction plot between *w* and *l*. By increasing *w* from 100 μm to 200 μm and decreasing *l* from 1,200 μm to 900 μm, *CSA* improved by approximately 53%. However, this change caused an undesirable increase in *FS* from 3% to 11%. In contrast to the requirements for *CSA*, narrow, long struts were ideal for reducing *FS*, as the struts deformed less to achieve an equivalent level of plastic strain, thereby reducing the level of axial contraction. This is in agreement with Li et al. [39] who acknowledged the contrasting requirements for *l*, based on the observed trade-off between recoil and *FS*. Strut thickness has the weakest effect on *CSA*—whilst a higher value of t reduced the degree of radial recoil post-inflation, it was not offset by the reduced *CSA* (as a result of the thicker struts) pre-inflation. In general, it was beneficial to design the stent such that it is stiffer in the circumferential direction (higher A_r) as *FS* improved without negatively affecting *CSA*. Hence, a lower value of *l* and A_r were desirable.

4.2 Cross-sectional area *vs*. stent-to-artery ratio

The trade-off between *CSA* and *SAR* was primarily due to the conflicting requirements for *w*. Although high values of *w* improved *CSA*, a wider strut increased the surface area of the stent which negatively affects *SAR*. Low values of *l* were correlated with improved *CSA*, and were also correlated with improved *SAR* as, intuitively, a shorter strut reduced the surface area of the stent. The interaction between *w* and *l* had the strongest effect on *SAR* (Fig 8c) and was evident from the response surface plot (Fig 13c). Stent-to-artery ratio was unaffected by *t* and A_r and hence, it was beneficial to design the stent with high values of A_r and *t* as these parameters improved *CSA*. High values of A_r and *t*, combined with a low value of *l* are ideal for improving both *CSA* and *SAR*. By holding each of these design parameters constant at their optimal limits and increasing *w* from 100 μm to 200 μm, *CSA* improved by approximately 20%. However, *SAR* had an undesirable increase from 22% to 40%, which is significantly higher than the *SAR* for both polymer and metallic stents in clinical practice, and may contribute to increased levels of thrombosis [12,13].

4.3 Foreshortening *vs*. radial collapse pressure

The trade-off between *FS* and *RCP* was primarily due to the conflicting requirements for *w*, *t* and *l*. Radial collapse pressure was most strongly affected by the interactions between *w* and *t*, *w* and *l* and *t* and *l*, with each interaction considered statistically significant ($p < 0.05$) (Fig 8d). The response surface plots for each of these interactions (Figs 12d, 13d and 14d) showed that *RCP* improves with high values of *t* and *w*, combined with low values of *l*. This combination of parameters tended to induce higher levels of plastic deformation in the strut hoops. By

increasing w and t from 100 μm to 200 μm and decreasing l from 1,200 μm to 900 μm, *RCP* improved from 8.8 kPa to 70 kPa, meeting the minimum allowable collapse pressure of 40 kPa [18]. However, this change caused an undesirable increase in *FS* from 2.5% to 12%. In general, A_r did not strongly affect *RCP* and was not considered statistically significant ($p > 0.05$). However, given that a higher A_r improved *FS*, it was beneficial to design the stent such that it is stiffer in the circumferential direction.

4.4 Stent-to-artery ratio *vs*. radial collapse pressure

The trade-off between *SAR* and *RCP* is similar to the trade-off observed between *SAR* and *CSA*, and is primarily due to the conflicting requirements for w. High values of A_r and t, combined with a low value of l are ideal for improving both *RCP* and *SAR*. By holding each of these design parameters constant at their optimal limits and increasing w from 100 μm to 200 μm, *RCP* had a more than three-fold increase. However, SAR had an undesirable increase of approximately 80%.

4.5 Limitations

In this study, stent geometries were based on a conventional open-cell design with straight bridges, which has proved ideal for metallic drug-eluting stents. However, this does not guarantee compatibility when using a polymer such as *PLLA* as the platform material, given that it exhibits an entirely different stress-strain response. Modifying the bridge geometry, strut cross-section and hinge profile have all been shown to influence the mechanical performance of stents [40,52] and the inclusion of these parameters may permit the evaluation of unconventional (or unorthodox) geometries that are better suited to polymeric stents. In addition to increasing the number of design parameters, the inclusion of a stenosed artery into the finite element model would permit additional performance metrics to be evaluated. Modelling the expansion of a stent in a stenosed artery could provide an indication of high risk areas in the stented region and may also be used to evaluate the stent's susceptibility to fracture. However, increasing the number of design parameters and performance metrics will increase the computational cost and complexity of the optimisation. Given that the performance metrics and design parameters evaluated within the present study were considered most critical based on the literature reviewed, any alternatives should be evaluated as additions rather than replacements. Finally, there is limited information in literature on clinically acceptable values for performance metrics such as foreshortening and stent-to-artery ratio. Identification of operational limits for these metrics is essential, as these limits can be used as constraints for the multi-objective optimisation procedure to tailor stent designs for a particular lesion or patient geometry, suggesting an area for future research.

5. Conclusion

An optimisation framework has been proposed that considers the combined effect of the biaxial stretching processing history and the geometric configuration when optimising the mechanical performance of a *PLLA* coronary stent. Response surface methodology combined with multi-objective optimisation produced an optimal *PLLA* stent design that offered improved performance relative to a baseline design for the same strut thickness (150 μm). The effects of each of the design parameters (A_r, w, t and l) on individual performance metrics (*CSA*, *FS*, *SAR* and *RCP*) have been quantified and compared. For each of the design parameters, a main factor or two-way interactions term had a statistically significant ($p < 0.05$) effect on at least one of the performance metrics. Pareto fronts highlighted that a change in one design parameter that improves one metric often leads to a compromise in at least one of the

other metrics with trade-offs observed for *CSA vs. FS*, *CSA vs. SAR*, *FS vs. RCP* and *SAR vs. RCP*. In summary, this study addresses key limitations in polymeric stent design and the computational framework detailed herein has potential application in the design of high stiffness, thin strut polymeric stents.

Acknowledgments

The authors wish to acknowledge the research institutions involved in the Bi-Stretch-4-Biomed collaborative RISE project (California Institute of Technology, University of Warwick and ENEA: Italian National Agency for New Technologies, Energy and Sustainable Economic Development).

Author Contributions

Conceptualization: Gary H. Menary.

Data curation: Ross W. Blair.

Formal analysis: Ross W. Blair.

Funding acquisition: Gary H. Menary.

Investigation: Ross W. Blair.

Methodology: Ross W. Blair, Nicholas J. Dunne, Alex B. Lennon, Gary H. Menary.

Project administration: Ross W. Blair.

Resources: Ross W. Blair.

Software: Ross W. Blair.

Supervision: Nicholas J. Dunne, Alex B. Lennon, Gary H. Menary.

Validation: Ross W. Blair.

Visualization: Ross W. Blair.

Writing – original draft: Ross W. Blair, Nicholas J. Dunne, Alex B. Lennon, Gary H. Menary.

Writing – review & editing: Ross W. Blair, Nicholas J. Dunne, Alex B. Lennon, Gary H. Menary.

References

1. Grüntzig A., 1978. Transluminal dilatation of coronary-artery stenosis. *The Lancet*, 311(8058):263.
2. Sigwart U., Puel J., Mirkovitch V., Joffre F. and Kappenberger L., 1987. Intravascular stents to prevent occlusion and re-stenosis after transluminal angioplasty. *New England Journal of Medicine*, 316 (12):701–706. https://doi.org/10.1056/NEJM198703193161201 PMID: 2950322
3. Windecker S., Mayer I., De Pasquale G., Maier W., Dirsch O., De Groot P. et al., 2001. Stent coating with titanium-nitride-oxide for reduction of neointimal hyperplasia. *Circulation*, 104(8):928–933. https://doi.org/10.1161/hc3401.093146 PMID: 11514381
4. Iqbal J., Onuma Y., Ormiston J., Abizaid A., Waksman R. and Serruys P., 2013. Bioresorbable scaffolds: rationale, current status, challenges, and future. *European Heart Journal*, 35(12):765–776. https://doi.org/10.1093/eurheartj/eht542 PMID: 24366915
5. Morice M. C., Serruys P. W., Sousa J. E., Fajadet J., Ban Hayashi E., Perin M. et al., 2002. A randomized comparison of a sirolimus-eluting stent with a standard stent for coronary revascularization. *New England Journal of Medicine*, 346(23):1773–1780. https://doi.org/10.1056/NEJMoa012843 PMID: 12050336

6. Stettler C., Wandel S., Allemann S., Kastrati A., Morice M. C., Schömig A. et al., 2007. Outcomes associated with drug-eluting and bare-metal stents: a collaborative network meta-analysis. *The Lancet*, 370(9591):937–948.
7. Bavry A. A., Kumbhani D. J., Helton T. J., Borek P. P., Mood G. R. and Bhatt D. L., 2006. Late thrombosis of drug-eluting stents: a meta-analysis of randomized clinical trials. *The American Journal of Medicine*, 119(12):1056–1061. https://doi.org/10.1016/j.amjmed.2006.01.023 PMID: 17145250
8. Kang S. H., Chae I. H., Park J. J., Lee H. S., Kang D. Y., Hwang S. S. et al., 2016. Stent thrombosis with drug-eluting stents and bioresorbable scaffolds: evidence from a network meta-analysis of 147 trials. *JACC*: *Cardiovascular Interventions*, 9(12):1203–1212. https://doi.org/10.1016/j.jcin.2016.03.038 PMID: 27262860
9. van Beusekom H. M., Saia F., Zindler J. D., Lemos P. A., Hoor S. L. S. T., van Leeuwen M. A. et al., 2007. Drug-eluting stents show delayed healing: paclitaxel more pronounced than sirolimus. *European Heart Journal*, 28(8):974–979. https://doi.org/10.1093/eurheartj/ehm064 PMID: 17434882
10. Gomez-Lara J., Garcia-Garcia H. M., Onuma Y., Garg S., Regar E., De Bruyne B. et al., 2010. A comparison of the conformability of everolimus-eluting bioresorbable vascular scaffolds to metal platform coronary stents. *JACC*: *Cardiovascular Interventions*, 3(11):1190–1198. https://doi.org/10.1016/j.jcin.2010.07.016 PMID: 21087756
11. Serruys P. W., Garcia-Garcia H. M. and Onuma Y., 2011. From metallic cages to transient bioresorbable scaffolds: change in paradigm of coronary revascularization in the upcoming decade? *European Heart Journal*, 33(1):16–25. https://doi.org/10.1093/eurheartj/ehr384 PMID: 22041548
12. Kawamoto H., Jabbour R. J., Tanaka A., Latib A. and Colombo A., 2016. The bioresorbable scaffold: will oversizing affect outcomes? *JACC*: *Cardiovascular Interventions*, 9(3):299–300. https://doi.org/10.1016/j.jcin.2015.11.019 PMID: 26847123
13. Kolandaivelu K., Swaminathan R., Gibson W. J., Kolachalama V. B., Nguyen-Ehrenreich K. L., Giddings V. L. et al., 2011. Stent Thrombogenicity Early in High-Risk Interventional Settings Is Driven by Stent Design and Deployment and Protected by Polymer-Drug Coatings. *Circulation*, 123(13):1400–1409. https://doi.org/10.1161/CIRCULATIONAHA.110.003210 PMID: 21422389
14. Kastrati A., Mehilli J., Dirschinger J., Dotzer F., Schühlen H., Neumann F. J. et al., 2001. Intracoronary stenting and angiographic results: strut thickness effect on restenosis outcome (ISAR-STEREO) trial. *Circulation*, 103(23):2816–2821. https://doi.org/10.1161/01.cir.103.23.2816 PMID: 11401938
15. Serruys P. W., Chevalier B., Sotomi Y., Cequier A., Carrié D., Piek J. J. et al., 2016. Comparison of an everolimus-eluting bioresorbable scaffold with an everolimus-eluting metallic stent for the treatment of coronary artery stenosis (ABSORB II): a 3 year, randomised, controlled, single-blind, multicentre clinical trial. *The Lancet*, 388(10059):2479–2491.
16. Ako J., Bonneau H. N., Honda Y. and Fitzgerald P. J., 2007. Design criteria for the ideal drug-eluting stent. *The American Journal of Cardiology*, 100(8):S3–S9.
17. Lim D., Cho S. K., Park W. P., Kristensson A., Ko J. Y., Al-Hassani S. T. S. et al., 2008. Suggestion of potential stent design parameters to reduce restenosis risk driven by foreshortening or dogboning due to non-uniform balloon-stent expansion. *Annals of Biomedical Engineering*, 36(7):1118–1129. https://doi.org/10.1007/s10439-008-9504-1 PMID: 18437572
18. Agrawal C. M., Haas K. F., Leopold D. A. and Clark H. G., 1992. Evaluation of poly (L-lactic acid) as a material for intravascular polymeric stents. *Biomaterials*, 13(3):176–182. https://doi.org/10.1016/0142-9612(92)90068-y PMID: 1567942
19. McMahon S., Bertollo N., O'Cearbhaill E. D., Salber J., Pierucci L., Duffy P. et al., 2018. Bio-resorbable polymer stents: a review of material progress and prospects. *Progress in Polymer Science*, 83:79–96.
20. Pauck R. G. and Reddy B. D., 2015. Computational analysis of the radial mechanical performance of PLLA coronary artery stents. *Medical Engineering and Physics*, 37(1):7–12. https://doi.org/10.1016/j.medengphy.2014.09.014 PMID: 25456397
21. Ang H. Y., Bulluck H., Wong P., Venkatraman S. S., Huang Y. and Foin N., 2017. Bioresorbable stents: Current and upcoming bioresorbable technologies. *International Journal of Cardiology*, 228:931–939. https://doi.org/10.1016/j.ijcard.2016.11.258 PMID: 27912202
22. Grogan J. A., Leen S. B. and McHugh P. E., 2012. Comparing coronary stent material performance on a common geometric platform through simulated bench testing. *Journal of the Mechanical Behavior of Biomedical Materials*, 12:129–138. PMID: 22705476
23. Menown I. B., Noad R., Garcia E. J. and Meredith I., 2010. The platinum chromium element stent platform: from alloy, to design, to clinical practice. *Advances in Therapy*, 27(3):129–141. https://doi.org/10.1007/s12325-010-0022-9 PMID: 20437213
24. Schmidt W., Behrens P., Brandt-Wunderlich C., Siewert S., Grabow N. and Schmitz K. P., 2016. In vitro performance investigation of bioresorbable scaffolds–standard tests for vascular stents and beyond. *Cardiovascular Revascularization Medicine*, 17(6):375–383. PMID: 27266902

25. Schmidt, W., Behrens, P. and Schmitz, K. P., 2009. Biomechanical aspects of potential stent malapposition at coronary stent implantation. Proceedings of the World Congress on Medical Physics and Biomedical Engineering, pages 136–139.

26. Bobel A. C., Petisco S., Sarasua J. R., Wang W. and McHugh P. E., 2015. Computational bench testing to evaluate the short-term mechanical performance of a polymeric stent. *Cardiovascular Engineering and Technology*, 6(4):519–532. https://doi.org/10.1007/s13239-015-0235-9 PMID: 26577483

27. Bergström J. S. and Hayman D., 2015. An overview of mechanical properties and material modeling of polylactide (PLA) for medical applications. *Annals of Biomedical Engineering*, 44(2):330–340. https://doi.org/10.1007/s10439-015-1455-8 PMID: 26369638

28. Alexy R. D. and Levi D. S., 2013. Materials and manufacturing technologies available for production of a pediatric bioabsorbable stent. *BioMed Research International* 2013.

29. Wu J. H., Yen M. S., Wu C. P., Li C. H. and Kuo M. C., 2013. Effect of biaxial stretching on thermal properties, shrinkage and mechanical properties of poly (lactic acid) films. *Journal of Polymers and the Environment*, 21(1):303–311.

30. Blair R. W., Dunne N. J., Lennon A. B. and Menary G. H., 2018. Processing-property relationships of biaxially stretched poly(L-lactic acid) sheet for application in coronary stents. *Journal of the Mechanical Behavior of Biomedical Materials*, 86:113–121. https://doi.org/10.1016/j.jmbbm.2018.06.017 PMID: 29986286

31. Bedoya J., Meyer C. A., Timmins L. H., Moreno M. R. and Moore J. E., 2006. Effects of stent design parameters on normal artery wall mechanics. *Journal of Biomechanical Engineering*, 128(5):757–765. https://doi.org/10.1115/1.2246236 PMID: 16995763

32. Migliavacca F., Petrini L., Colombo M., Auricchio F. and Pietrabissa R., 2002. Mechanical behavior of coronary stents investigated through the finite element method. *Journal of Biomechanics*, 35(6):803–811. PMID: 12021000

33. Pant S., Limbert G., Curzen N. P. and Bressloff N. W., 2011. Multiobjective design optimisation of coronary stents. *Biomaterials*, 32(31):7755–7773. https://doi.org/10.1016/j.biomaterials.2011.07.059 PMID: 21821283

34. Lally C., Dolan F. and Prendergast P. J., 2005. Cardiovascular stent design and vessel stresses: a finite element analysis. *Journal of biomechanics*, 38(8):1574–1581. https://doi.org/10.1016/j.jbiomech.2004.07.022 PMID: 15958213

35. Bressloff N. W., Ragkousis G. and Curzen N., 2016. Design optimisation of coronary artery stent systems. *Annals of Biomedical Engineering*, 44(2):357–367. https://doi.org/10.1007/s10439-015-1373-9 PMID: 26183960

36. Barragan P., Rieu R., Garitey V., Roquebert P. O., Sainsous J., Silvestri M. et al., 2000. Elastic recoil of coronary stents: a comparative analysis. *Catheterization and Cardiovascular Interventions*, 50(1):112–119. PMID: 10816295

37. Ota T., Ishii H., Sumi T., Okada T., Murakami H., Suzuki S. et al., 2014. Impact of coronary stent designs on acute stent recoil. *Journal of Cardiology*, 64(5):347–352. https://doi.org/10.1016/j.jjcc.2014.02.013 PMID: 24679906

38. García A., Peña E., and Martínez M. A., 2012. Influence of geometrical parameters on radial force during self-expanding stent deployment. Application for a variable radial stiffness stent. *Journal of the Mechanical Behavior of Biomedical Materials*, 10:166–175. https://doi.org/10.1016/j.jmbbm.2012.02.006 PMID: 22520428

39. Li H., Wang X., Wei Y., Liu T., Gu J., Li Z. et al., 2017. Multi-Objective Optimizations of Biodegradable Polymer Stent Structure and Stent Microinjection Molding Process. *Polymers*, 9(1):20.

40. Pant S., Bressloff N. W., and Limbert G., 2011. Geometry parameterization and multidisciplinary constrained optimization of coronary stents. *Biomechanics and Modeling in Mechanobiology*, 11(1–2):61–82. https://doi.org/10.1007/s10237-011-0293-3 PMID: 21373889

41. Timmins L. H., Moreno M. R., Meyer C. A., Criscione J. C., Rachev A. and Moore J. E., 2007. Stented artery biomechanics and device design optimization. *Medical and Biological Engineering and Computing*, 45(5):505–513. https://doi.org/10.1007/s11517-007-0180-3 PMID: 17375345

42. Bobel A. C. and McHugh P. E., 2018. Computational Analysis of the Utilisation of the Shape Memory Effect and Balloon Expansion in Fully Polymeric Stent Deployment. *Cardiovascular Engineering and Technology*, 9(1):60–72. https://doi.org/10.1007/s13239-017-0333-y PMID: 29243163

43. Blair R. W., Dunne N. J., Lennon A. B. and Menary G. H. Characterisation and constitutive modelling of biaxially stretched poly(L-lactic acid) sheet for application in coronary stents. *Journal of the Mechanical Behavior of Biomedical Materials*, 97:346–354. https://doi.org/10.1016/j.jmbbm.2019.05.039 PMID: 31153116

44. Bobel A. C., Lohfeld S., Shirazi R. N. and McHugh P. E., 2016. Experimental mechanical testing of Poly (l-Lactide) (PLLA) to facilitate pre-degradation characteristics for application in cardiovascular stenting. *Polymer Testing*, 54:150–158.

45. Abbott, 2012. Absorb Bioresorbable Vascular Scaffold System, Abbott Vascular, 3200 Lakeside Drive, Santa Clara, CA 95054–2807, USA.

46. Morris M. D., Mitchell T. J., 1995. Exploratory designs for computational experiments. *Journal of Statistical Planning and Inference*, 43:381–402.

47. R Core Team, 2017. *R*: *A Language and Environment for Statistical Computing*, R Foundation for Statistical Computing, Vienna, Austria. Retrieved from: https://www.r-project.org/ [Accessed 19 Feb. 2018].

48. Hunter J. D., 2007. Matplotlib: A 2D Graphics Environment, *Computing in Science & Engineering*, 9:90–95.

49. Oliphant, T. E, 2006. A guide to NumPy, USA: Trelgol Publishing. Retrieved from: http://www.numpy.org [Accessed 5 Dec. 2018].

50. Jones E., Oliphant E. and Peterson P., 2001. SciPy: Open Source Scientific Tools for Python. Retrieved from: http://www.scipy.org/ [Accessed 6 Feb. 2019].

51. Wang W. Q., Liang D. K., Yang D. Z. and Qi M., 2006. Analysis of the transient expansion behavior and design optimization of coronary stents by finite element method. *Journal of Biomechanics*, 39(1):21–32. https://doi.org/10.1016/j.jbiomech.2004.11.003 PMID: 16271584

52. Grogan J. A., Leen S.B. and McHugh P. E., 2013. Optimizing the design of a bioabsorbable metal stent using computer simulation methods. *Biomaterials*, 34(33):8049–8060. https://doi.org/10.1016/j.biomaterials.2013.07.010 PMID: 23906516